

# The influence of the 3D Galactic gas structure on cosmic-ray transport and $\gamma$ -ray emission

Andrés Ramírez<sup>1</sup>, Gordian Edenhofer<sup>2,3</sup>, Torsten A. Enßlin<sup>2,3,6</sup>, Philipp Frank<sup>2</sup>, Philipp Mertsch<sup>4</sup>,  
Vo Hong Minh Phan<sup>5</sup>, Laurin Söding<sup>4</sup>, Hanieh Zhandinejad<sup>2,3</sup>, and Ralf KISSmann<sup>1</sup>

<sup>1</sup> Universität Innsbruck, Institut für Astro- und Teilchenphysik, Technikerstr. 25/8, 6020 Innsbruck, Austria  
e-mail: Andres.Ramirez-Tapias@uibk.ac.at

<sup>2</sup> Max Planck Institute for Astrophysics, Karl-Schwarzschild-Straße 1, 85748 Garching bei München, Germany

<sup>3</sup> Ludwig Maximilian University of Munich, Geschwister-Scholl-Platz 1, 80539 München, Germany

<sup>4</sup> Institute for Theoretical Particle Physics and Cosmology, RWTH Aachen University, Sommerfeldstr. 16, 52074 Aachen, Germany

<sup>5</sup> Sorbonne Université, Observatoire de Paris, PSL Research University, LERMA, CNRS UMR 8112, 75005 Paris, France

<sup>6</sup> Excellence cluster ORIGINS, Boltzmannstr. 2, 85748 Garching, Germany

## ABSTRACT

*Context.* Cosmic rays (CRs) play a major role in the dynamics of the interstellar medium (ISM). Their interactions and transport ionize, heat, and push the ISM thereby coupling different regions of it. The spatial distribution of CRs depends on the distribution of their sources as well as the ISM constituents they interact with, such as gas, starlight, and magnetic fields. Particularly, gas interacts closely with CRs, influencing CR fluxes and  $\gamma$ -ray emission.

*Aims.* We illustrate the influence of 3D gas structures on CR transport and  $\gamma$ -ray emission.

*Methods.* We use the PICARD code and multiple samples of recent 3D reconstructions of the HI and H<sub>2</sub> Galactic gas constituents to investigate the impact on the transport of CRs and emission of  $\gamma$ -rays.

*Results.* We find the necessary transport parameters to reproduce local measurements of CR fluxes, and see that they depend on the local distribution of gas density and structure. The distribution of CR fluxes exhibits energy-dependent structures that vary for all CR species due to their corresponding loss processes. Regions of enhanced secondary (primary) species are spatially correlated (anti-correlated) with the gas density. We observe a high sensitivity of the  $\gamma$ -ray emission on the contrast of gas structures, as those determine the 3D spatial distributions of hadronic interactions and bremsstrahlung. We find that corresponding gas-induced structures in the distribution of CR electrons are also visible in Inverse Compton (IC) emission. Due to the aforementioned sensitivity, the analysis of CR data for CR sources and transport parameters requires the usage of accurate 3D gas maps.

**Key words.** Diffusion – Methods: numerical – cosmic rays – ISM: kinematics and dynamics – Gamma rays: ISM

## 1. Introduction

Cosmic rays (CRs) are an important component of the Galactic interstellar medium (ISM). They interact with other constituents of the ISM such as gas, dust, turbulent magnetic fields and interstellar radiation. Furthermore, CRs are believed to affect the chemical and dynamical evolution of the ISM from small (star-forming) to large, Galactic scales (Padovani et al. 2020; Gabici 2022; Phan et al. 2023; Simpson et al. 2023). Several studies suggest that CRs drive Galactic winds and, thus, could play an essential role in the evolution history of the Milky Way (MW) (Farcy et al. 2022; Girichidis et al. 2022).

Despite the importance of CRs in the Galactic ecosystem, the transport of these particles is still far from being fully understood. Analyses of CR secondary-to-primary ratios (e.g. B/C and <sup>10</sup>Be/<sup>9</sup>Be) indicate that these particles propagate diffusively within a magnetized halo (with a typical height of around 3-6 kpc) surrounding the Galactic disk (Evoli et al. 2020; Maurin et al. 2022; Jacobs et al. 2023). The diffusion of CRs is thought to be due to their interactions with magnetic turbulence (the turbulent component of the Galactic magnetic field). In this respect, Galactic CR modelling formally follows from coupling the transport of CRs to magnetic turbulence (Schlickeiser 2002; Blasi 2013), using a set of non-linear coupled differential equations.

Solving these coupled equations remains challenging in many different ways. For example, it is not yet clear whether magnetic turbulence is predominantly generated from the cascade of large-scale turbulence injected by supernova explosions or from CRs themselves via the streaming instability (Skilling 1975; Nava et al. 2016; Jacobs et al. 2022). Several recent analyses, in fact, indicate that both mechanisms are important (Thomas & Pfrommer 2019; Thomas et al. 2020) and in different energy ranges they lead to features in the CR spectra (Génolini et al. 2017; Evoli et al. 2018). Another difficulty in modelling Galactic CR transport and magnetic turbulence self-consistently is our lack of knowledge on the large-scale magnetic field of the MW (Beck 2015). More precise 3D models of the Galactic magnetic field (Jansson & Farrar 2012a,b) would be essential for a better understanding of CR propagation (Haverkorn et al. 2019) since the diffusion coefficients of CRs parallel and perpendicular to the field lines are expected to differ, making the Galactic distribution of CRs sensitive to the exact geometry of the large-scale magnetic field (Cerri et al. 2017; Mertsch 2020; Giacinti & Semikoz 2023).

Given all the above-mentioned complexities, the propagation of CRs is normally modelled in a linear fashion, via the CR transport equation assuming parametric forms of the diffusion coefficients and other transport and acceleration parameters such as

the advection speed (due to plasma waves or Galactic winds) or the diffusion coefficient in momentum space (for the process of re-acceleration). In fact, the growing amount of high-precision CR data has led to the development and refinement of multiple sophisticated CR transport and interaction codes such as GALPROP (Porter et al. 2022), DRAGON (Evoli et al. 2017), USINE (Maurin 2020) and PICARD (Kissmann 2014). These codes provide numerical or semi-analytical solutions for the CR transport equation, taking into account many different physical processes not only for transport but also for particle acceleration and interactions between CRs and the ISM (resulting in energy loss and production of secondary CRs via spallation). The combination of these transport codes and high-precision CR data (Adriani et al. 2014, 2022; Aguilar et al. 2023), covering energy ranges from the MeV to the TeV scale and beyond, has been extensively used to extract corresponding transport and acceleration parameters (Strong et al. 2007a; Grenier et al. 2015; Gabici et al. 2019).

In many of these CR transport codes, gas distributions are, however, modelled through the introduction of axisymmetric Galacto-centric models. Since gas serves as a target for spallation reactions of primary CRs producing secondary CRs, approximate 2D gas distributions and more realistic 3D ones are expected to yield different estimates for secondary-to-primary ratios for otherwise identical transport parameters. Conversely, different estimates of the transport parameters are expected between 2D and 3D gas models when inferring them from data on CR secondary-to-primary ratios. This is observed when a more structured 3D model is used for the inference of transport parameters instead of a smooth axisymmetric model, yielding a lower diffusion coefficient  $D_{\text{xx}}$  and a reduced Alfvén speed  $v_A$  (see e.g., Jóhannesson et al. (2018), but also Table 1 here).

Furthermore, interactions between CRs and gas can result in observable diffuse  $\gamma$ -ray emissions, i.e. via decays of  $\pi^0$  (produced in hadronic interactions of CRs with interstellar gas nuclei) or via bremsstrahlung by CR electrons. Diffuse  $\gamma$ -ray data can, therefore, be used to derive the Galactic distribution of CRs assuming models for the 3D gas distributions (Ackermann et al. 2012; Tibaldo et al. 2021). Despite their relevance, 3D gas distributions are still not commonly used in studies of Galactic CR transport.

One of the main methods for deriving 3D gas distributions is to analyze data of spectral emission and absorption lines. Atomic hydrogen (HI), for instance, can be traced through the 21-cm emission line. Since gas at different locations along a line of sight in general has different relative velocities with respect to the observer due to Galactic rotation, it emits this line at different Doppler-shifted frequencies. This means that, given a model for Galactic rotation, data of this emission line can be used to reconstruct a model for the 3D distribution of HI. A similar approach can be applied to the  $J = 1 \rightarrow 0$  emission line of  $^{12}\text{CO}$  to trace molecular hydrogen ( $\text{H}_2$ ) assuming a conversion factor between  $^{12}\text{CO}$  and  $\text{H}_2$  gas density. However, given our vantage point in the Galaxy, many of these reconstructed gas maps suffer from a number of ambiguities. For instance, the peculiar motion of gas (i.e. random motions of gas, on top of the large-scale rotational gas flow caused e.g. by stellar winds and supernova explosions) introduce artificial structures stretching along the lines of sight into the 3D gas reconstructions, known as the finger-of-god effect (see e.g., Nakanishi & Sofue 2003, 2006; Pohl et al. 2008). Recently it has been suggested that this problem can be cured by taking the spatial correlations of gas into account (Mertsch, P. & Vittino, A. 2021; Mertsch, P. & Phan, V. H. M. 2023). Incorporating spatial correlations into 3D gas reconstructions turns those into high-dimensional Bayesian inference problems. Such have

been addressed via information field theory (Enßlin et al. 2009; Enßlin 2019) in Mertsch, P. & Vittino, A. (2021) and Mertsch, P. & Phan, V. H. M. (2023) by using the NIFTy package<sup>1</sup> (Selig et al. 2013; Steininger et al. 2019; Arras et al. 2019; Edenhofer et al. 2024). This has not only provided improved 3D gas reconstructions but also quantified their remaining uncertainties.

In this work, we aim to study how the 3D gas structures, as seen in such improved 3D gas reconstructions, influence CR transport and  $\gamma$ -ray emission. We model this by introducing 3D reconstructed maps into diffusive CR transport simulations. For comparison, we also produce an axisymmetric version of the same 3D reconstructed maps. We use both models to infer transport parameters, and to simulate the energy-dependent spatial distribution of CRs and of  $\gamma$ -ray emission with the PICARD code.

The structure of the remainder of this work is as follows. In section 2, we detail how the reconstruction and axisymmetric models are introduced into the PICARD simulation setups. Then, in section 3 we discuss the morphological features induced by the 3D gas on simulated CR transport and  $\gamma$ -ray emission, and compare the resulting CR spectra and transport parameter estimates between 2D ring and 3D models. Finally, in section 4 we summarize our results and present our conclusions.

## 2. Methodology

In the PICARD code, a steady state solution to the CR transport equation for each nucleus is obtained on a numerical grid either using axisymmetric cylindrical coordinates or a three-dimensional Cartesian grid in space – as described for our models below – and one energy dimension, where we use a logarithmically equidistant axis, ranging from 10 MeV to 1 PeV in 127 grid points. Our setup is based on previous axisymmetric models from Ackermann et al. (2012), i.e. their model  $^{\text{S}}\text{Y}^{\text{Z}}4^{\text{R}}20^{\text{T}}150^{\text{C}}5$ . In particular, we are using the axisymmetric cosmic-ray source distribution by Yusifov & Küçük (2004), which we truncated beyond a Galactocentric radius of 15 kpc as also discussed in Kissmann et al. (2015). The transport parameters are the same as in  $^{\text{S}}\text{Y}^{\text{Z}}4^{\text{R}}20^{\text{T}}150^{\text{C}}5$  apart from Alfvén speed and normalisation and energy dependence of spatial diffusion, as discussed below. Additionally, the models for the magnetic field and the radiation field are also axisymmetric as also used in Ackermann et al. (2012). Correspondingly, the new three-dimensional gas reconstructions are the only non-axisymmetric components considered in the transport equation. We use the same set of spallation cross-sections and energy loss process as GALPROP v54<sup>2</sup> (see e.g., Strong & Moskalenko 1998; Moskalenko & Strong 1998; Moskalenko et al. 2002).

Nuclei are coupled through spallation reactions which lead to corresponding loss and source terms. For the handling of the related nuclear network see Kissmann et al. (2015). Thus, for particles resulting from interactions with Galactic gas,  $n_{\text{Tot}}$  defines the interaction regions producing secondaries.

We adapt the recently reconstructed 3D maps of molecular ( $\text{H}_2$ ) (Mertsch, P. & Vittino, A. 2021) and atomic (HI) (Mertsch, P. & Phan, V. H. M. 2023) hydrogen into the PICARD simulations. These reconstructions were performed following two different gas flow models, namely BEG03 (based on the results of a smoothed particle hydrodynamics simulation) and SBM15 (based on a semi-analytical model for gas-carrying orbits) as introduced in the original articles. Since we are interested in the

<sup>1</sup> [github.com/NIFTy-PPL/NIFTy](https://github.com/NIFTy-PPL/NIFTy)

<sup>2</sup> [galprop.stanford.edu/download/manuals/galprop\\_v54.pdf](https://galprop.stanford.edu/download/manuals/galprop_v54.pdf)

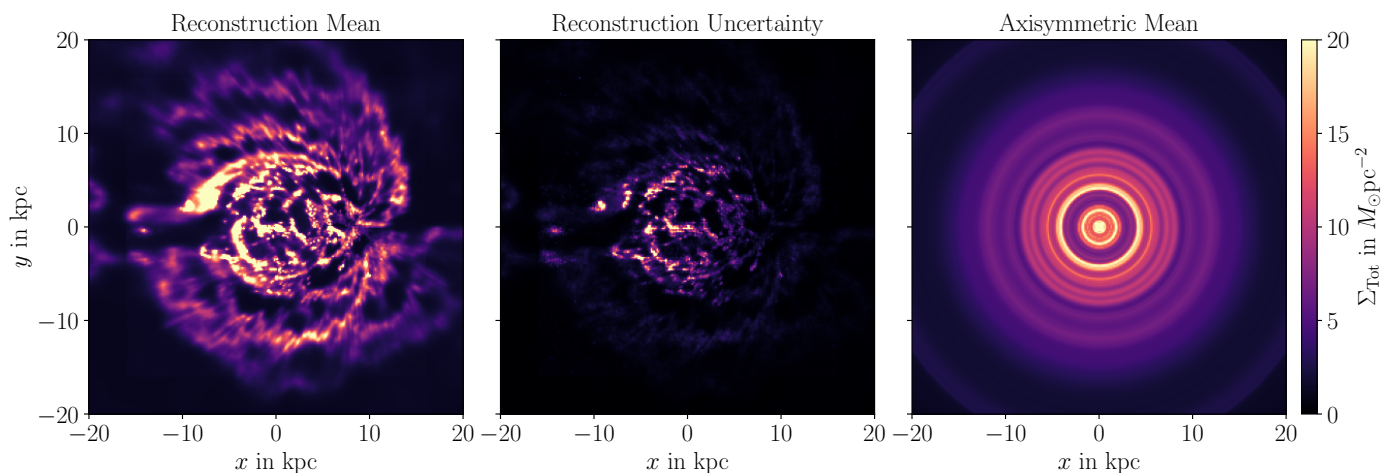


**Fig. 1.** *Left:* surface mass density for the reconstruction mean map of the 3D gas model. *Middle:* corresponding uncertainty for the constituent sample maps. *Right:* surface column density for the axisymmetric map of the 2D model.

**Table 1.** Transport parameters used for the two different setups.

Parameter	2D model	3D model
<i>General</i>		
Halo height [kpc]		4
Galactic radius [kpc]		20
Diffusion coefficient $D_{xx}$ <sup>1</sup> [ $10^{24}$ m <sup>2</sup> /s]	5.10	3.90
Reference Rigidity $R_0$ [GV]		4
Diffusion coefficient index $a_1$ below $R_0$ <sup>2</sup>	0.26	0.21
Diffusion coefficient index $a_2$ above $R_0$ <sup>2</sup>	0.38	0.40
Alfvén speed $v_A$ [ $10^3$ m/s]	31.0	21.0
<i>Nuclei injection spectrum</i>		
Index below break		1.89
Index above break		2.39
Break energy [GeV]		11.41
<i>Nuclei normalisation</i>		
Normalisation energy [GeV]		108
Normalisation flux <sup>a</sup>		$4 \cdot 10^{-2}$
<i>Electron injection spectrum</i>		
Index below 1 <sup>st</sup> break		1.6
Index between 1 <sup>st</sup> and 2 <sup>nd</sup> break		2.425
Index above 2 <sup>nd</sup> break		4.0
1 <sup>st</sup> break energy [GeV]		1
2 <sup>nd</sup> break energy [GeV]		$2.5 \cdot 10^3$
<i>Electron normalization</i>		
Normalisation energy [GeV]		25
Normalisation flux <sup>a</sup>		$1.09 \cdot 10^{-2}$

<sup>1</sup>  $D_{xx} = \beta(R/R_0)^a$

<sup>a</sup> Normalisation flux given in units of [ $\text{m}^{-2}\text{s}^{-1}\text{sr}^{-1}(\text{GeV}/\text{nucleon})^{-1}$ ]

distribution of 3D structures, both are equally good candidates for the purpose of this work. Here, we selected the HI and H<sub>2</sub> maps based on the BEG03 gas flow model. These maps come in the form of 32 H<sub>2</sub> and 16 HI independent posterior sample maps. Out of the 512 possible combinations of H<sub>2</sub> and HI sample pairs, we subsample by randomly choosing 20 map pairs to account for fluctuations in the gas structure. To load each pair of gas maps into the simulations, we interpolate them from their original reconstruction grid onto the PICARD simulation grid. The gas maps are then added with the analytical model of ionised

(HII) gas used in PICARD to generate the total distribution of protons in the galaxy  $n_{\text{Tot}}$ . This is calculated as

$$n_{\text{Tot}}(\mathbf{r}) = 2n_{\text{H}_2}(\mathbf{r}) + n_{\text{HI}}(\mathbf{r}) + n_{\text{HII}}(\mathbf{r}) \quad (1)$$

From these maps we produce two simulation setups. For the first one, from hereon referred to as the 2D model, we average over the selected sample maps to produce a reconstruction mean map. We interpolate this map from the reconstruction grid to a cylindrical grid  $(r, \phi, z)$ . To produce an axisymmetric model, we

average the result over the azimuth  $\phi$ . The resulting 2D distribution is given on a grid with 128 grid points in the  $r$  dimension and 65 grid points in the  $z$  dimension. The grid spans from 0 kpc to 20 kpc in  $r$  and from -4 kpc to 4 kpc in  $z$ . For the second setup, from hereon referred to as the 3D model, we interpolate the 20 samples directly onto the Cartesian simulation grid  $(x, y, z)$ . This grid is defined by 257 grid points in both  $x$  and  $y$  dimensions spanning the same range from -20 kpc to 20 kpc. The  $z$  axis is identical to the one in the 2D model. As a result, both configurations possess the same resolution.

Both setups are illustrated in Fig 1 where we show the resulting surface mass density ( $\Sigma_{\text{Tot}}$ ) of the reconstruction mean map and the uncertainty (e.g one standard deviation) computed over the samples, as well as the surface mass density of the 2D model map.

Different gas models cause the simulated secondary to primary ratios at Earth to differ when compared to data (i.e. B/C ratio data). To understand these differences, we heuristically calibrate our transport parameters by modifying those related to the strength and speed of CR diffusion. Namely, the diffusion coefficient  $D_{xx}$ , its corresponding indices  $a_1$  and  $a_2$ , and the Alfvén speed  $V_A$ . We perform this calibration by running multiple simulations with slightly different values for the parameters thereof, until finding a rough by-eye agreement between the simulated B/C ratios and AMS-02 data (Aguilar et al. 2018). We do this for both the 2D and 3D models using the axisymmetric and reconstruction mean maps shown in Fig. 1, respectively. In this work, the heaviest element considered in the simulations is Silicon, where contributions from heavier elements are neglected, as they impact the distribution of Carbon and Boron isotopes by less than a percent. The resulting set of transport parameters are presented in Table 1.

Nuclei are coupled through spallation reactions which lead to corresponding loss and source terms. For the handling of the related nuclear network see Kissmann et al. (2015). Thus, for particles resulting from interactions with Galactic gas,  $n_{\text{Tot}}$  defines the interaction regions producing secondaries.

Diffuse  $\gamma$ -ray emission is computed considering the contributions from  $\pi^0$ -decay, bremsstrahlung, and IC scattering. For this calculation, transport results for relevant CR species (hydrogen, helium, electrons and positrons) are used with the corresponding cross-sections to generate emissivities at the specified energies of interest (see e.g, Strong & Moskalenko 1998; Strong et al. 2000). For  $\pi^0$ -decay and bremsstrahlung, specific emissivities are produced which are later multiplied with the total proton distribution to obtain the final  $\gamma$ -ray emissivities in the Galaxy. For these simulations, the spatial grid is the same as in the transport step and CR energies range from 10 GeV to 1 TeV in 10 logarithmically equidistant grid points. After the diffuse emission is computed, the specific emissivities for  $\pi^0$ -decay and bremsstrahlung are interpolated onto a Cartesian grid with the same spatial resolution as the sample maps, to multiply them with the total gas distribution. Such grid preserves the full resolution of the sample maps, spanning the same dimensions as that of the 3D model, with (640,640,128) grid points in the  $(x, y, z)$  dimensions. From the local emission, all-sky  $\gamma$ -ray emission follows via line-of-sight (LOS) integration.

### 3. Results and Discussion

The main results of our simulations are the energy-dependent spatial distributions of Galactic CR fluxes ( $J(E)$ ) and of local  $\gamma$ -ray emissivities ( $\epsilon(E)$ ) – as well as the LOS integrals of the latter – computed with the 3D model. In this section, we present

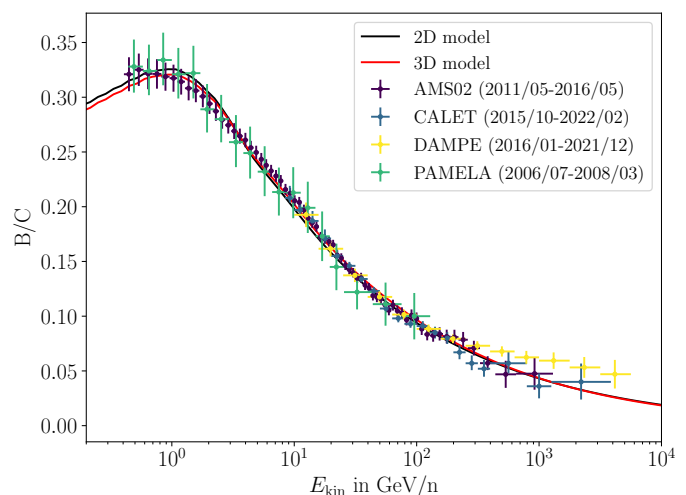


**Fig. 2.** B/C ratio fit for 2D and 3D models at Earth compared to AMS-02 (Aguilar et al. 2018), CALET (Adriani et al. 2022), DAMPE (Dampe Collaboration 2022) and PAMELA (Adriani et al. 2014) data. The ratio is shown with a heliospheric modulation of 678.6 MV estimated for the AMS-02 measurement.

the summary statistics of these results and compare them, where applicable, to the morphology of the gas reconstruction maps and the results obtained by using the 2D model. All uncertainties shown here correspond to the  $1\text{-}\sigma$  region of the simulation outputs. For all our results related to CR nuclei fluxes we define the energy axis by their corresponding kinetic energy per nucleon (n). We denote this convention as  $E_{\text{kin}}$  in GeV/n units. For leptons, we use their corresponding kinetic energy  $E_{\text{kin}}$  in GeV units.

#### 3.1. Impact on Transport Parameters

Boron nuclei are predominantly produced via the interaction of heavier nuclei (e.g. Carbon and oxygen) with ISM gas. The relative abundances between secondary and primary nuclei are sensitive to the mechanisms of CR transport, making their measurement an important probe to constrain the parameters involved in CR propagation (Strong et al. 2007b; DAMPE Collaboration 2022). Particularly, Boron and Carbon abundances are extensively well documented. Therefore, we use the available B/C ratio data to investigate the constraints introduced in the transport parameters related to diffusion, given the usage of the gas reconstructions. In Fig 2 we show the fits to the B/C ratio data resulting from the calibration of the transport parameters described in section 2. We note that the 2D model requires  $D_{xx}$  and  $v_A$  values slightly above typical values (see e.g., Strong et al. 2007b, where  $D_{xx} \sim (3 - 5) \times 10^{24} \text{ m}^2 \text{ s}^{-1}$  and  $v_A \sim 30 \text{ km s}^{-1}$ ).

The transport parameters of the 3D model deviate significantly from the ones in the 2D model by requiring a smaller diffusive strength to remain close to the AMS-02 data. This behaviour is related to the gas density near Earth in both models. We check this behavior in each model by evaluating the corresponding average hydrogen densities  $\bar{n}$  within a sphere of 4kpc radius around the location of Earth. For the 2D model,  $\bar{n}_{2D}(|\mathbf{r} - \mathbf{r}_{\text{Earth}}| \leq 4\text{kpc}) \approx 62 \times 10^{-3} \text{ cm}^{-3}$  and for the 3D model,  $\bar{n}_{3D}(|\mathbf{r} - \mathbf{r}_{\text{Earth}}| \leq 4\text{kpc}) \approx 53 \times 10^{-3} \text{ cm}^{-3}$ . We find that  $\bar{n}_{2D} \approx 1.17\bar{n}_{3D}$  in this region, leading to  $D_{xx2D} \approx 1.31D_{xx3D}$  and  $v_{A2D} \approx 1.48v_{A3D}$ . Consequently, we observe a direct correlation between the average gas density in the vicinity of Earth and with  $D_{xx}$  and  $v_A$ , where smaller average gas densities require weaker

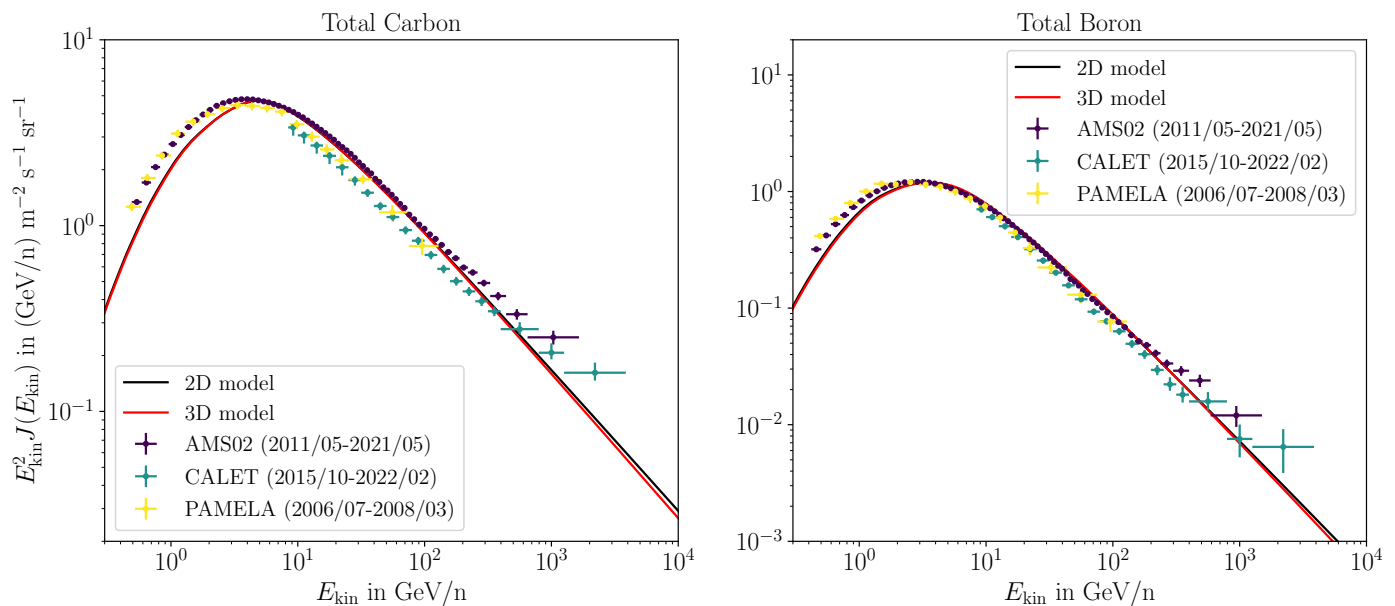


**Fig. 3.** Carbon and Boron spectra for the 2D and 3D models at Earth compared to AMS-02 (Aguilar et al. 2023), CALET (Adriani et al. 2022) and PAMELA (Adriani et al. 2014) data. The spectra are shown with a heliospheric modulation of 587.9 MV estimated for the AMS-02 measurement.

diffusion and reacceleration. However, we note that changes in  $n_{3D}$  do not translate linearly to changes in  $D_{xx}$  and  $v_A$ , this results from gas structures at different scales affecting the flux of CRs via their interactions (e.g. spallation, energy losses), which we discuss further in section 3.3.

In Fig 3, we present the simulated Carbon and Boron spectra at Earth that constitute the fitted B/C ratio, as well as corresponding observations. The main deviations between data and simulated spectra are present for energies below 10 GeV/n, where at the estimated heliospheric modulation, the simulated fluxes are below the data. Stable Boron isotopes (i.e.  $^{10}\text{B}$  and  $^{11}\text{B}$ ) are mainly produced from spallations of CR  $^{12}\text{C}$  and of CR  $^{16}\text{O}$  with ISM protons, which also produce unstable Carbon isotopes that decay further (see Table 1 in Heinbach & Simon (1995) for the related cross-sections). This anti-correlates the population of Boron and Carbon non-linearly, where the latter is dominated by the  $^{12}\text{C}$  (see e.g. Fig 6). As a result, given enough local gas density, we expect a greater gain of Boron nuclei isotopes from a lower loss of Carbon nuclei., Twhich can explain therefore, the relative deviations from the data beingare larger for Carbon than for Boron result from the sensitivity of the distribution of CRs to both the choice of transport parameters and the local gas density. We also note that for these models – in order to account to the change in slope to fit AMS-02 data – the diffusion coefficient indices  $a_1$  and  $a_2$  deviate from the standard Kolmogorov spectrum index  $a = 0.33$ .

### 3.2. Impact on CR distributions

All nuclei are subject to spallation in dense gas regions during transport, resulting in the production of secondary lighter nuclei at the expense of the interacting primary. As a consequence of this effect, simulations display under-populated regions that appear for primary nuclei where high density gas regions are located. In contrast, for secondaries over-populated regions appear at high gas density regions. Hence, particles of mainly primary (secondary) nature are anti-correlated (correlated) with the distribution of gas. We illustrate this morphological impact of

the 3D model on the distribution of different CR species. For this purpose, we look at the flux distributions at  $\sim 10$  GeV/n and  $\sim 1$  TeV/n of: Carbon 12 ( $^{12}\text{C}$ ), Boron 10 ( $^{10}\text{B}$ ), primary and secondary protons, and primary and secondary electrons (see sections 3.2.1, 3.2.2 and 3.2.3, respectively).

To compare the differences between 2D and 3D models across all energies, we further investigate the CR spectra from the 2D model and the mean CR spectra from the 3D model, for the same species as listed before. For all spectra shown henceforth, we use the set of transport parameters given in Table 1 for the 3D model.

We calculate spectra at the Galactic center (GC) and at Earth’s location, where the latter is fixed by the underlying velocity field model used to reconstruct the 3D gas density. For the BEG03 model, Earth is assumed to be located at 8.0 kpc from the GC. We choose the GC region to study the impact of the distribution of gas structures, given that the average gas density within any distance  $r$  from the GC is the same between the 2D and 3D models. For spectra at Earth we compare with CR data, where we use the force-field approximation to model heliospheric modulation. We take the modulation potential (see e.g., Ghelfi et al. 2017, for details on its estimation) from the AMS-02 measurements, as reported in the cosmic ray database (CRDB) (Maurin et al. 2014, 2020, 2023).

#### 3.2.1. Boron and Carbon

In Fig 4, we show the mean and uncertainty of the distribution of  $^{12}\text{C}$  and  $^{10}\text{B}$  fluxes in the Galactic plane, at 9.64 GeV/n and 1.04 TeV/n energies. For  $^{12}\text{C}$ , being mainly a primary CR particle, we note that under-populated regions are correlated with dense gas regions. This effect is most notable at 9.64 GeV/n near the GC, where the under-populated region follows the same profile as the dense gas region seen at the same location in Fig 1 for the 3D model. Furthermore, the under-populated regions disappear with increasing energy, becoming barely visible at 1.04 TeV/n and staying only at the densest gas regions. This result depends on the CR species and is a consequence of

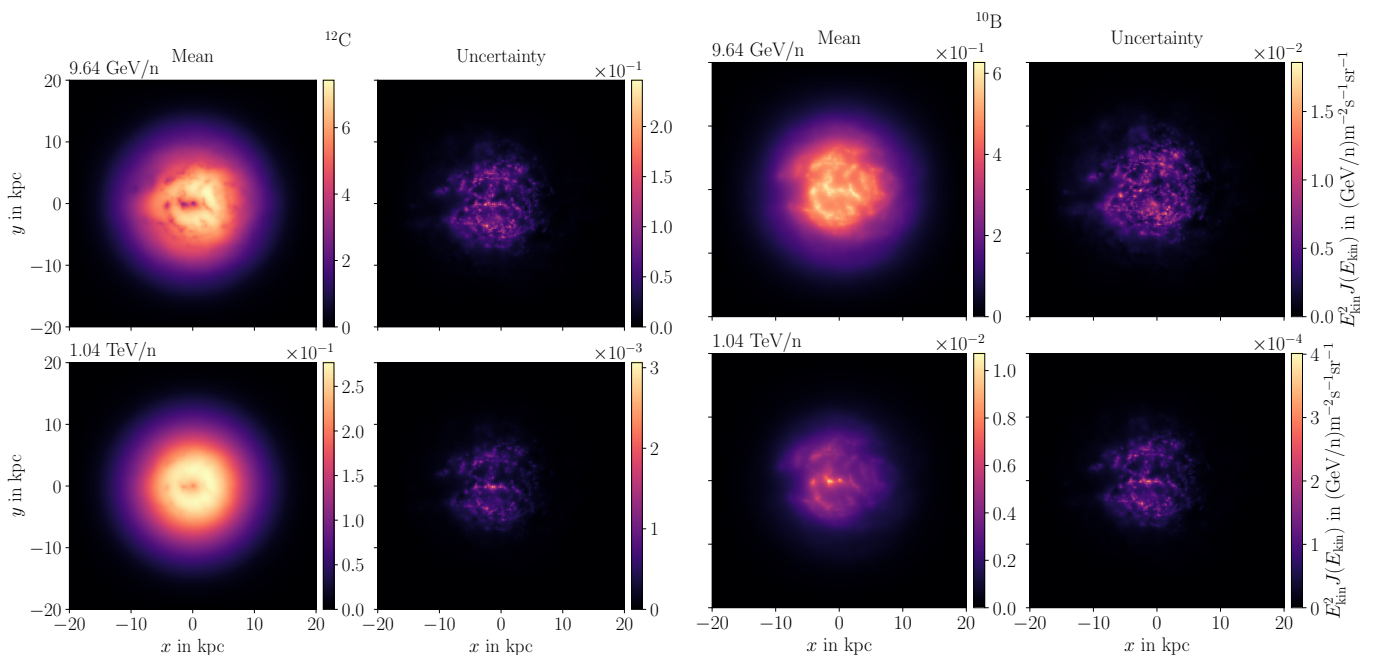


**Fig. 4.** *Left:* Galactic plane view of  $^{12}\text{C}$  mean distributions (left column) and uncertainties (right column) for the 3D model. *Right:* Same for  $^{10}\text{B}$ . These quantities are presented for each nucleus type at 9.64 GeV/n (top rows) and 1.04 TeV/n (bottom rows).

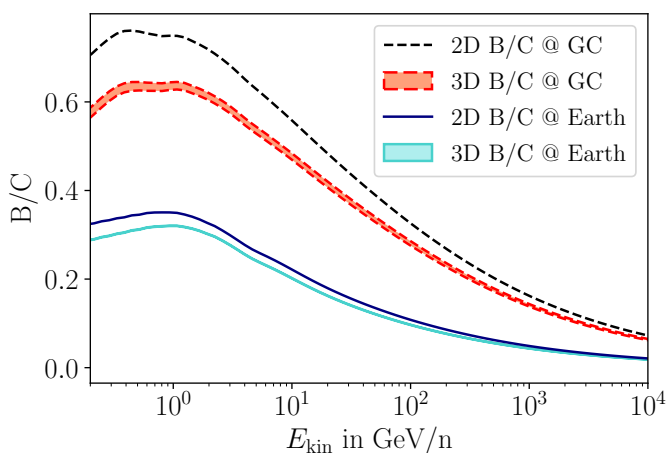


**Fig. 5.** B/C ratio for the 2D and 3D models using the 3D model parameters for both. The collection of all simulations in the 3D model is represented by the bands covering the  $1\text{-}\sigma$  region of our samples. We show the B/C ratio at Earth (dashed lines) and at the GC (solid lines), where results at Earth are shown with a heliospheric modulation of 678.6 MV.

the corresponding dominant interaction at the energy of interest. When energy increases, loss time scales (e.g. for spallation, energy losses) become much longer when compared to the escape time of CRs from the Galaxy due to diffusion, causing spatial structures to become smooth.

For  $^{10}\text{B}$ , being of purely secondary nature, we note that the over-populated regions are directly correlated to dense gas regions. In contrast to  $^{12}\text{C}$ , this correlation is not suppressed with increasing energies, despite diffusion dominating over other interactions. This is a consequence of the secondary CR nuclei production rate being proportional to the ISM gas density. Therefore, given that losses are also high in the high density regions, secondaries can not easily escape these regions by diffusion. We

discuss the relationship between gas and interaction rates further in section 3.3.

For the corresponding uncertainties, we observe that they follow a profile similar to the reconstruction uncertainty of the gas within 10 kpc from the GC, as shown in Fig 1. The gas reconstruction profile is more evident at 1.04 TeV/n, whereas at 9.64 GeV/n and more clearly for  $^{10}\text{B}$ , structures towards the GC are smeared out and do not resemble the gas reconstruction profile. Despite this, for both species, we note that the relative uncertainties are much smaller for the CR distributions than for the gas reconstruction, decreasing further as energy increases.

In Fig 5 we present the B/C ratio at Earth and at the GC for both the 2D and 3D models using the same set of transport parameters (i.e. those from the 3D model, as discussed above). At both locations, we observe a higher B/C ratio in the 2D model than in the 3D model, where we find a general over-population of Boron at all energies. We investigate the effects that lead to this increase from the individual Carbon and Boron spectra at Earth and at the GC, which we show in Fig 6. At Earth, the total Carbon spectrum for the 2D model shows a slight decrease below 30 GeV/n, converging to the same flux as in the 3D model above this energy. A slight hardening of the Boron spectrum is present in the 2D model above 10 GeV/n, while both models agree below this energy. This leads to the overall increase of the B/C ratio in the 2D model seen in Fig 5, when compared to the 3D model. At the GC, the Carbon flux for the 2D model is noticeably reduced up to an energy of 200 GeV/n with respect to the 3D model. For Boron, the 2D model exhibits a reduced flux up to an energy of 10 GeV/n with respect to the 3D case. At 10 GeV/n, the Boron spectra are harder in the 2D model, leading to more high-energy Boron produced at the GC than in the 3D model.

In general, we observe a common set of effects. All particles – albeit more strongly for primaries than for secondaries – possess a higher flux in the 3D model up to a certain energy. Secondary-particle fluxes are lower in the 3D model above a certain energy. The energy at which these fluxes change depends on the corresponding CR species, and the magnitude of these dif-

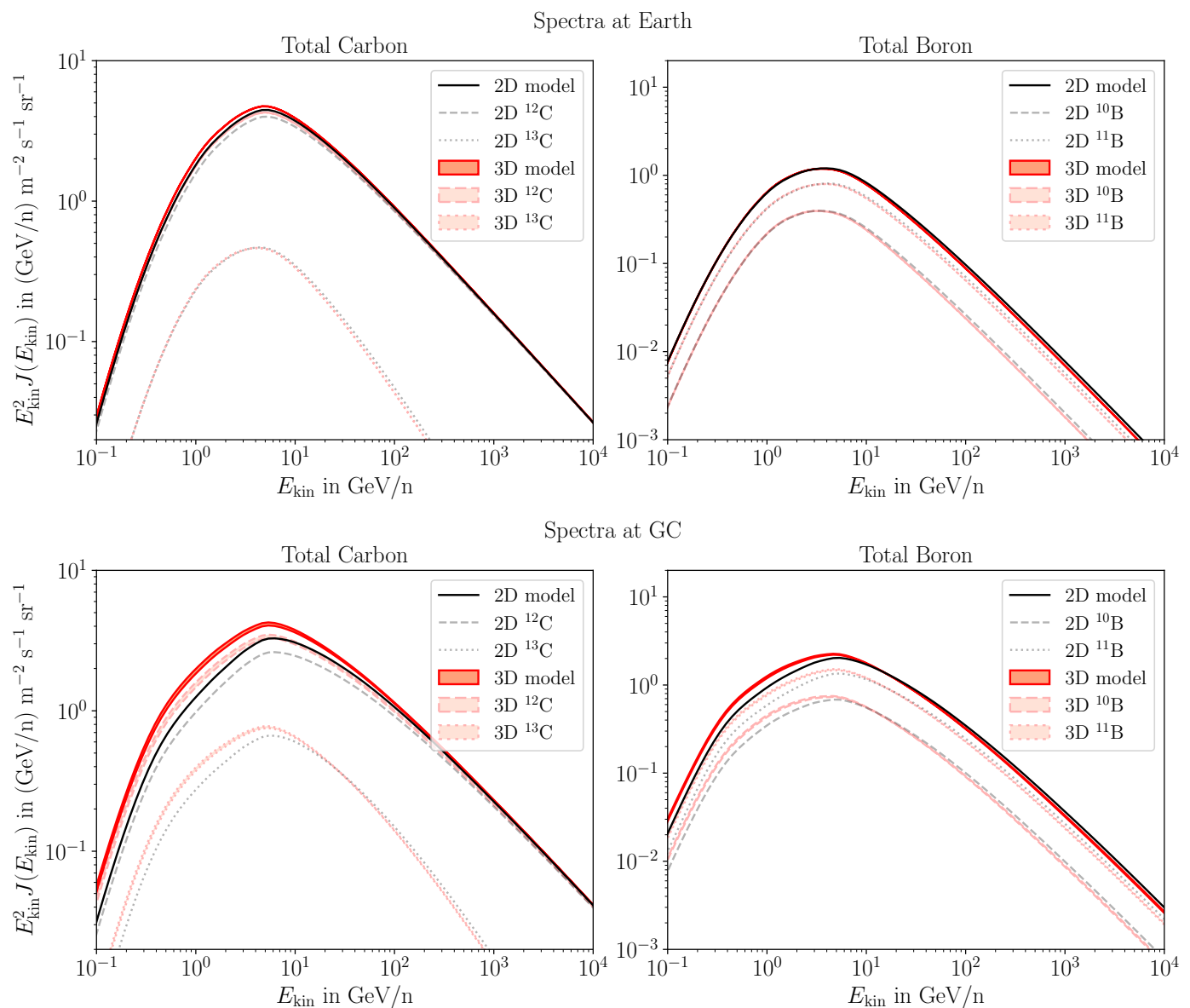


**Fig. 6.** Spectra for the total flux of Carbon (Left) and Boron (Right) in the 2D and 3D models at Earth (top) and at the GC (bottom). C and B spectra are shown as solid lines. Dashed and dotted lines are used for the constituent isotopes as indicated in the figures. For spectra at Earth we use a heliospheric modulation potential of 587.9 MV. Here, the 3D model parameters are used for both models.

ferences between models depends on the location, being more obvious when looking at locally dense gas regions. Therefore, the flux differences reflect the correlation between the distribution of gas with the mean-free-path a particle traverses, given the presence of local gas over-/under-densities through the particular path and sufficiently short interaction rates (see e.g., section 3.3 and Fig. 13 for the computation of this correlation). In particular for Boron and Carbon in the 3D model, this means that a higher flux of low-energy primaries is correlated to a lower flux of high-energy secondaries, since less spallation processes take place due to the local gas under-densities of a structured 3D model.

The dependence on the distribution of gas can be studied further by examining the spectra at the GC in Fig. 6. Here, the gas density is locally the same in both the 2D and 3D model. Therefore, loss processes contribute in the same way and the resulting differences in fluxes between models come as a direct consequence of the distribution of gas structures itself, instead of the

local average density. The differences are especially visible for the total Carbon spectra at energies below 10 GeV/n, where the flux for the 2D model is about 2 times smaller than the one for the 3D model. From Fig 1, we note that within 4 kpc of the GC in the map for the 2D model there is an under-dense ring to which CRs can diffuse with equal probability in any direction, whereas in the 3D model the local under-dense regions are located north and south of the GC, constraining the directions in which CRs can diffuse from the GC.

### 3.2.2. Primary and secondary protons

In Fig 7 we show the mean and uncertainty of the distribution of simulated protons in the Galactic plane where, similarly to the  $^{12}\text{C}$  and  $^{10}\text{B}$  cases, we find that the same correlation between primaries, secondaries and gas exists. In contrast, the distributions exhibit a different energy dependence, with far less structures visible for primary protons. As for the distribution of sec-

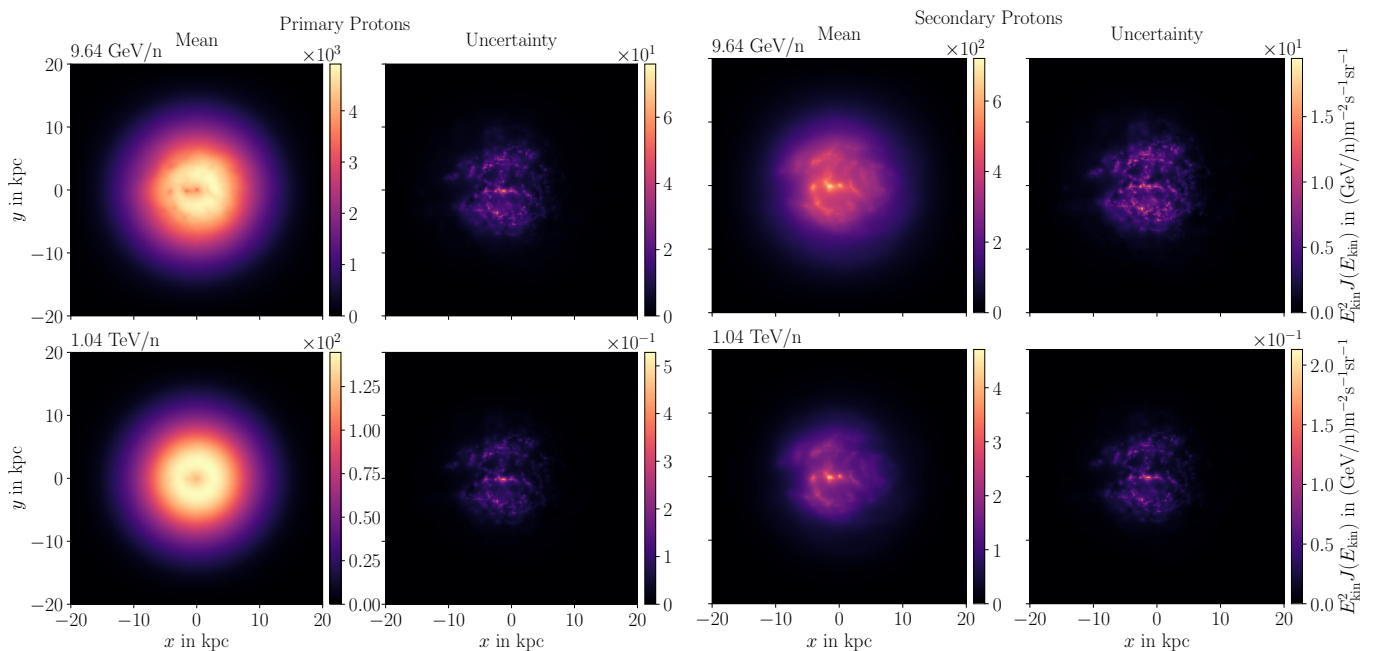


**Fig. 7.** Like Fig 4, but for primary and secondary protons.

ondaries, while still correlated to the gas density, it is less saturated at lower energies for protons. This is a consequence of the proton interactions (see e.g., Tan & Ng 1983) for the modeling of the relevant proton cross-section) being inherently different from the Carbon and Boron ones, making the imprint of the gas distribution on CR fluxes depending also on the corresponding CR species.

In Fig 8 we show the simulated proton spectra, where we note again the general effects discussed for Carbon and Boron. Here, the differences between models are negligible at Earth, which comes as a consequence of primary protons dominating the total flux, and being used for the normalization of the fluxes of all nuclei. With the differences between models being more noticeable at the GC than at Earth, and at energies where catastrophic and momentum losses in gas regions are significant, we observe again the structure-dependent behaviour of the simulated CR fluxes. We note as well that this dependence is only broken when diffusion dominates at high energies.

### 3.2.3. Primary and secondary electrons

The relationship between electrons and gas density differs from the CR species considered so far, due to their different energy loss processes. One important process is bremsstrahlung, which takes place in dense gas and can dominate electron losses between  $\sim$  hundred MeV and a few GeV, before becoming subdominant to IC losses due to interactions with the different components of interstellar radiation field (ISRF) (Evoli et al. 2020). As for the production of secondaries, this occurs via the decay of mesons produced in collisions of CR nuclei with gas, producing secondary electrons in dense gas regions. In Fig. 9 we show the mean distribution and standard deviation of the simulated electrons in the Galactic plane, where we see the same correlation structure discussed so far due to the interactions discussed before. Primary electron under-densities remain visible for the densest gas clouds at energies of up to  $\sim$  150 GeV. However, as energy increases losses due to IC and synchrotron emission become dominant, and no further gas structures are imprinted on

primaries. Consequently, given the high energy losses at TeV energies, very high energy electrons seem to not travel far from their sources – or gas for secondary electrons – (see e.g., Mertsch 2020; Evoli et al. 2021; Thaler et al. 2023), leading to a sharper outline of their structures with increasing energies, as seen at 1.04 TeV in comparison to 9.64 GeV.

We show the electron spectra at Earth and at the GC in Fig 10. Once again, we note the general effects pointed out for Carbon and Boron. Like for the primary proton case, lepton species are normalized using primary electrons, causing negligible differences between models at Earth. Furthermore, the discrepancy to AMS-02 data can be addressed by adapting the injection spectra of electrons that were used in the simulations. Particularly in the electron case, secondary species dominate the spectrum at very high energies, due to the softening of the primary injection spectrum. We see this effect clearly at  $\sim$  2 TeV at the GC.

### 3.3. Correlation Structure

Here, we display the correlation structure observed thus far in detail, by focusing on CR protons first to discuss how gas structures modulate their energy-dependent morphology. For this purpose, we study the proton interaction timescales at both the GC and Earth, the low-energy mean distribution of CR protons, and the correlation between gas and CR protons in the 3D model. As previously stated, energy-dependent spatial structures follow from the spatial distribution of gas via the corresponding interactions of the different particle species. When such interactions contribute significantly to CR losses in comparison to the escape rate of CRs from the Galaxy, the resulting CR distribution exhibits local structures that follow the gas maps. In Fig. 11, we show a comparison for protons between their inelastic, ionization and escape loss rates averaged over a sphere with radius 4 kpc around Earth. The escape rate is computed as  $1/\tau_{\text{Esc}} = D/H^2$  with  $H = 4$  kpc the halo height and  $D$  the rigidity-dependent diffusion coefficient, using the values for the 3D model in Table 1. To illustrate the impact of the gas distribution on the distribution of CR fluxes at lower energies, we show



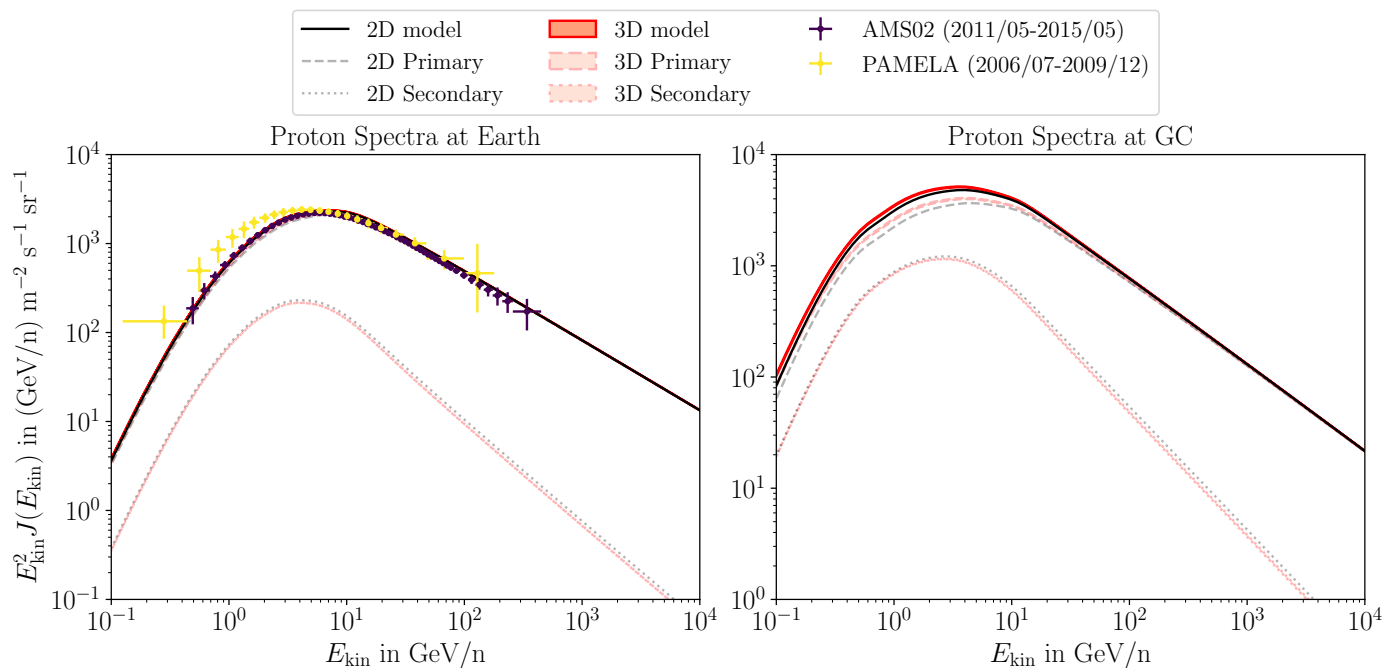


**Fig. 8.** *Left:* Simulated proton spectra at Earth for the 2D model and the 3D model. Primary and secondary components are shown via dashed and dotted lines respectively. *Right:* Same, but at the GC. Spectra at Earth are compared to AMS-02 (Aguilar et al. 2023) and PAMELA (Adriani et al. 2014) data, and shown with a heliospheric modulation of 684.9 MV. Here, the 3D model parameters are used for both models.

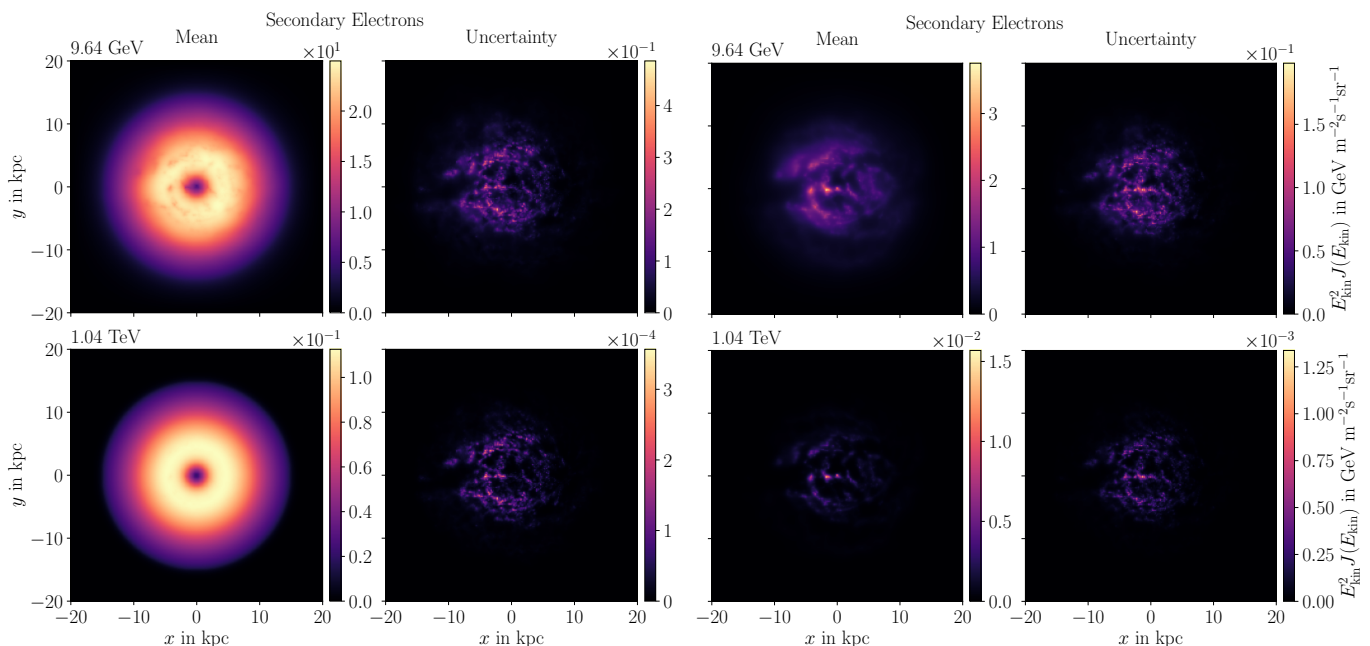


**Fig. 9.** Like Fig 4, but for primary and secondary electrons.

in Fig. 12 the Galactic plane distribution of primary and secondary protons at 108 MeV/n. Although ionization rates dominate the low energy regime, primary protons are still subject to inelastic losses, which in turn drive the production of secondaries. We note that the ionization losses dominate for energies lower than  $\approx 200$  MeV/n, resulting in decreased primary proton fluxes in most dense gas regions within 10 kpc of the GC. The under-dense features disappear at locations with sufficiently less dense gas as diffusion becomes dominant, leading to the smoothing of the distribution of primary protons visible in Fig. 7 for

the distributions 9.64 GeV/n and 1.04 TeV/n. We note that the gas-induced structures that are still visible at 9.64 GeV/n result due to inelastic losses being on a similar magnitude as diffusion. For secondaries, while the loss rates are the same, their injection occurs only at dense gas locations and thus their distribution is primarily determined by the gas maps.

To quantify this energy-dependent relationship between the structure of fluxes for primaries and secondaries, and that of the gas density, we calculate the Pearson correlation coefficient. For this, we use protons and electrons, and compare their distribution

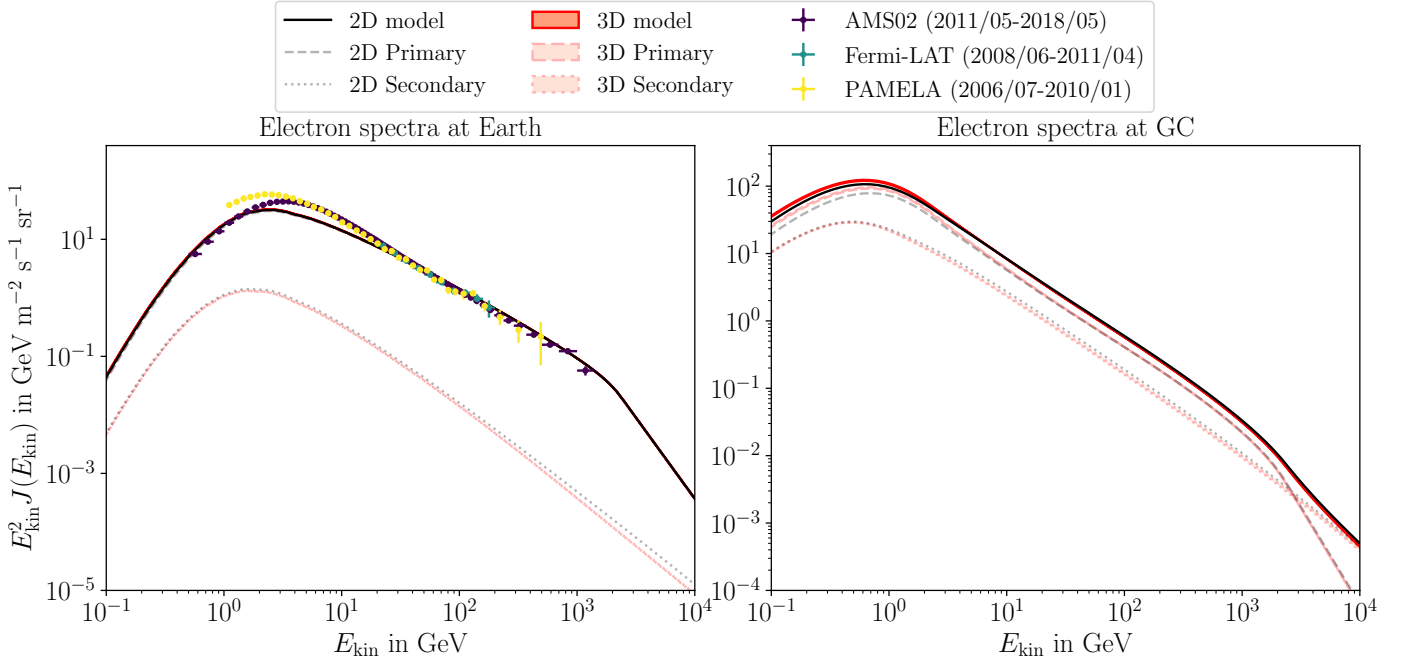


**Fig. 10.** Like Fig 8, but for primary and secondary electrons.

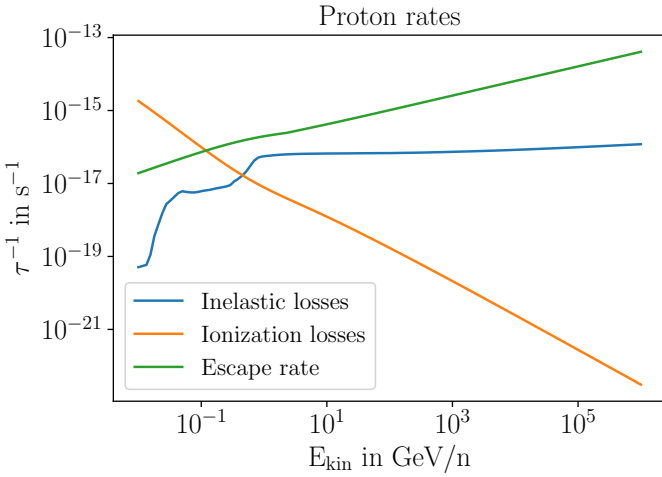


**Fig. 11.** Interaction rates for protons. Ionization and inelastic losses are proportional to the local gas density. Here,  $\bar{n}_{\text{gas}} = 0.05 \text{ cm}^{-3}$  within 4 kpc from Earth in the 3D model.

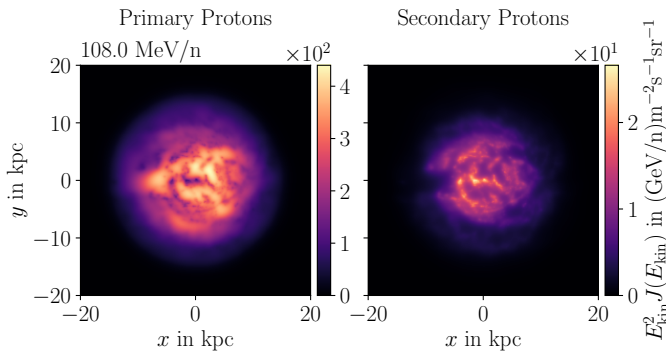


**Fig. 12.** Distribution of primary (left) and secondary (right) protons on the Galactic plane at 108 MeV/n.

with the gas distribution inside 2 regions of radius  $r = 0.5 \text{ kpc}$  and  $r = 3.5 \text{ kpc}$  around the GC in the Galactic plane. The  $0.5 \text{ kpc}$  region considers the small over-dense patch of gas at the very center of the Galaxy, while the  $r = 3.5 \text{ kpc}$  region takes into account local over- and under-dense gas clouds. The resulting energy-dependent correlation coefficients, along with the corresponding regions are shown in Fig. 13. We note the anti-correlation (correlation) between primaries (secondaries) and gas density in both regions at all energies. For very-high-energy secondary electrons (i.e.  $E_{\text{kin}} \geq 100 \text{ TeV/n}$ ) the correlation is very close to 1, reflecting an almost linear dependence between gas and secondary electrons as a consequence of their increasingly strong confinement to their source regions (i.e. the high density regions) due to their high energy losses. We observe that with increasing energies, the absolute value of the correlation coefficient between secondaries and gas is bigger than the one between primaries and gas. This comes as a consequence of the anti-correlation with primaries being driven by gas-dependent losses. On the  $r = 3.5 \text{ kpc}$  region, the correlation coefficient for secondary protons becomes considerably smaller, since they can travel larger distances than electrons due to lower energy losses.

### 3.4. Gamma-ray emission

Here, we show our  $\gamma$ -ray emission results, which are based only on the 3D model. Like for the CR transport results, we check the morphological impact of the 3D model on the individual emission channels. We identify their relation to the distribution of gas by studying the mean  $\gamma$ -ray spectra at different over-/underdense gas regions in the Galactic plane.

In Fig 14, we show the mean distributions and uncertainties of the simulated local emissivities for  $\pi^0$ -decay and bremsstrahlung  $\gamma$ -ray emission, as well as for the total  $\gamma$ -ray emission (including IC). We show these results in the Galactic plane at 10 GeV. The profile of the total  $\gamma$ -ray emission is directly correlated to dense gas regions as a consequence of  $\pi^0$ -decay being the dominant emission channel. Unlike the CR transport

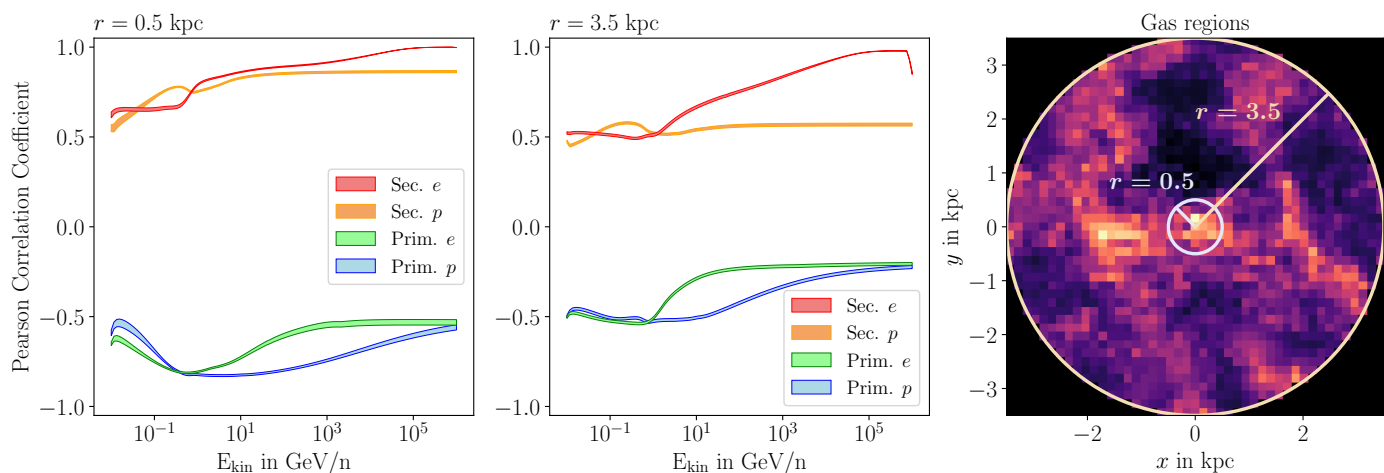


**Fig. 13.** Pearson correlation coefficient at all simulated energies between electrons/protons and gas. We compute the coefficients for the Galactic plane regions within 0.5 and 3.5 kpc from the GC. Each band covers the  $1\text{-}\sigma$  region over the 3D model simulations.

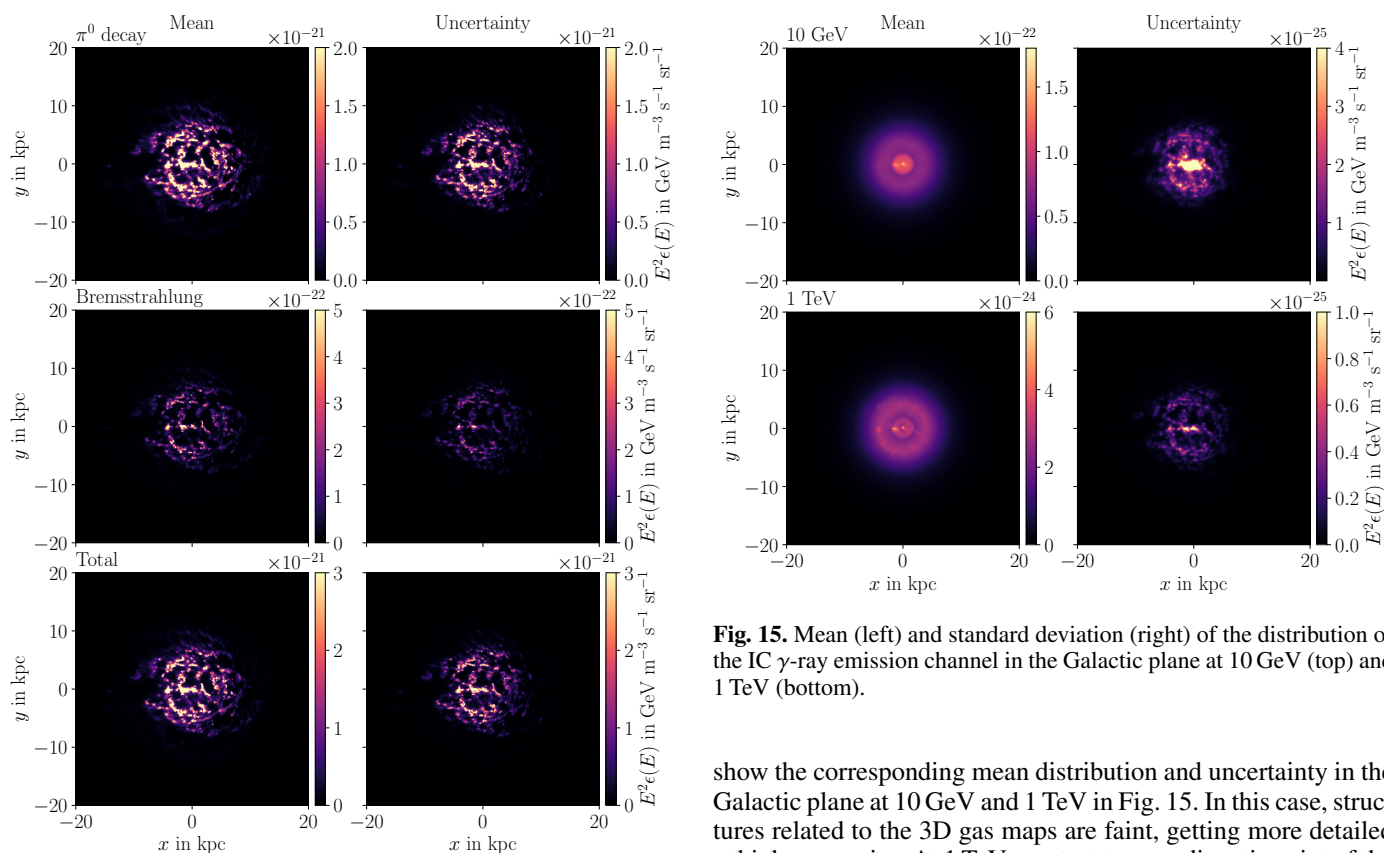


**Fig. 14.** Mean distribution (left) and standard deviation (right) of the  $\gamma$ -ray emission channels in the Galactic plane at 1 TeV. Emission channels from top to bottom:  $\pi^0$ -decay, bremsstrahlung and Total

case,  $\pi^0$ -decay and bremsstrahlung emission scale linearly with gas density, and the corresponding uncertainty is similar to the one of the gas reconstruction, in particular, at locations of high  $\text{H}_2$  density. Consequently,  $\pi^0$ -decay and bremsstrahlung emission exhibit uncertainties of magnitudes comparable to their corresponding mean distribution.

In contrast, IC emission follows from the interaction between CR electrons and the ISRF, where the latter is introduced in the simulations by a 2D model, as discussed in section 2. We

**Fig. 15.** Mean (left) and standard deviation (right) of the distribution of the IC  $\gamma$ -ray emission channel in the Galactic plane at 10 GeV (top) and 1 TeV (bottom).

show the corresponding mean distribution and uncertainty in the Galactic plane at 10 GeV and 1 TeV in Fig. 15. In this case, structures related to the 3D gas maps are faint, getting more detailed at higher energies. At 1 TeV we start to see a direct imprint of the gas distribution, which is visible at  $\sim 5$  kpc away from the GC in every direction. Unlike the other emission channels, IC emission does not scale linearly with the gas density. As a result, features on the emissivities only appear due to the existing structures in the distribution of CR electrons, which explains the uncertainties being negligible, as seen for the CR fluxes.

In Fig 16 we compare the  $\gamma$ -ray spectra from regions of varying gas density, where we show the simulated mean total  $\gamma$ -ray together with the corresponding uncertainties at different locations in the Galactic plane. We note that the emission is mostly proportional to the gas density, being highest at the GC. The uncertainties observed in  $\gamma$ -ray spectra are much larger than for the CR spectra and correlate directly with most regions with high gas density, where the uncertainties of the gas are also high-

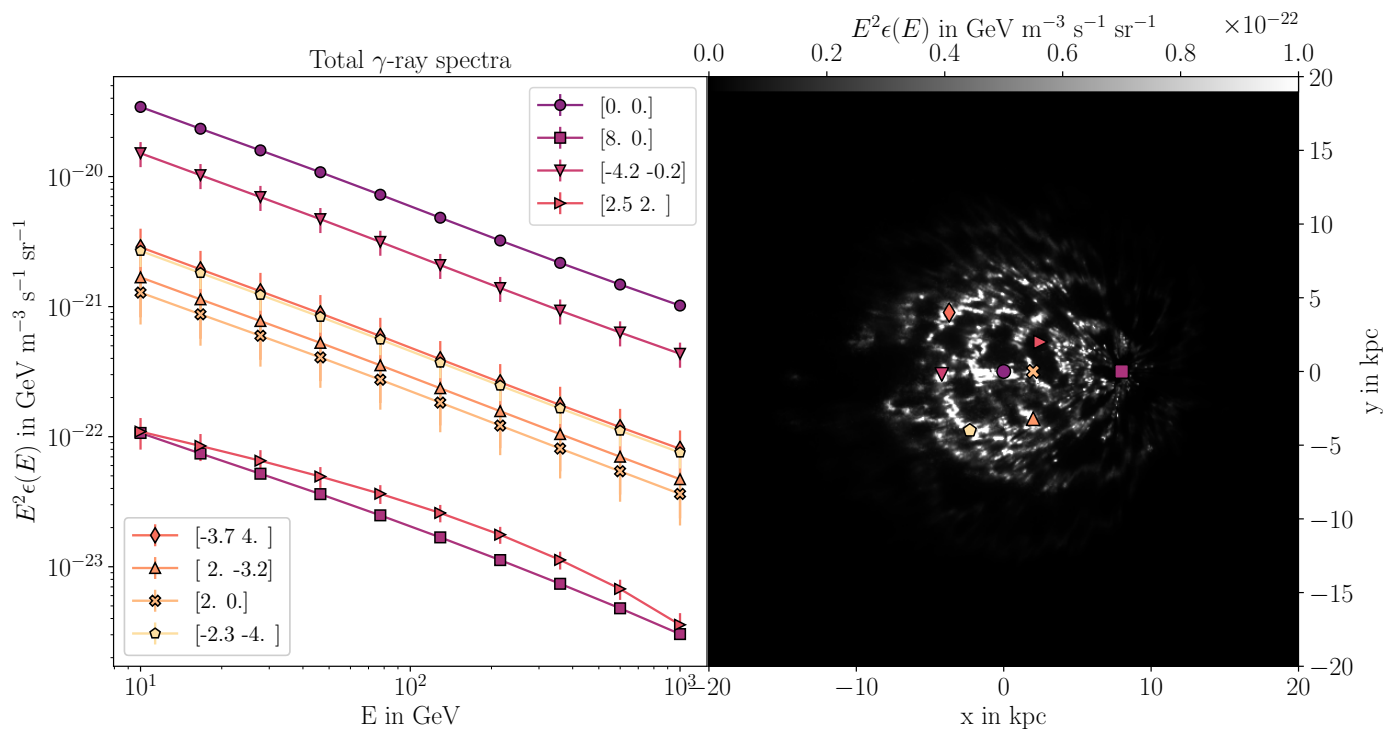


**Fig. 16.** Total  $\gamma$ -ray spectra simulated at specific locations of varying density in the Galactic plane.

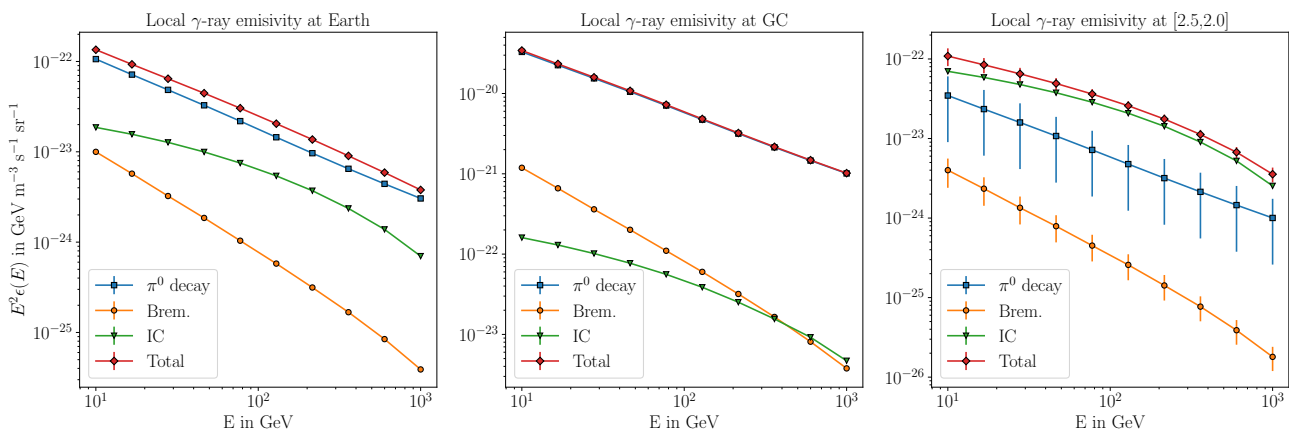


**Fig. 17.** Total and individual  $\gamma$ -ray spectra channels simulated at Earth's location (left), at the GC (middle) and in the under-dense region located at [2.5, 2, 0].

est. The emission is however not directly correlated to the gas density everywhere. This can be the case if the source density is locally enhanced. For instance, the low gas density location at  $(x, y, z) = (2.5, 2, 0)$  with  $n_{3D}(2.5, 2, 0) = 0.16 \text{ cm}^{-3}$  features a higher total  $\gamma$ -ray emission than in the vicinity of Earth with density  $n_{3D}(8, 0, 0) = 0.65 \text{ cm}^{-3}$ . We also find that at the aforementioned low density region, the total  $\gamma$ -ray emission exhibits a change in slope when compared to the emission at the other locations. This is a consequence of the individual emission channels, which we show in Fig. 17, where we find that the slope change is related to the locally dominant IC channel. The local dominance of IC emission is a consequence of the joint effect of the ISRF being high and a locally low gas density. At Earth,  $\pi^0$ -decay emission is dominant with IC emission becoming comparable in the 100–600 GeV energy range. At the GC, the gas density is so high bremsstrahlung emission dominates over IC emission. In our gas model we find a low uncertainty at the GC, which is a

consequence of the underlying velocity field model and leads to negligible uncertainties of  $\gamma$ -ray emission at this exact location.

In Fig 18, we show the LOS-integrated emission maps for all channels at 10 GeV and 1 TeV. We note that all major structures in the total emission follow from the dominating  $\pi^0$ -decay emission. For bremsstrahlung emission, contributions are concentrated in the Galactic plane where the gas density is highest. In contrast to its corresponding local emissivity, the LOS-integrated IC emission exhibits no gas structures. Furthermore, IC emission extends to higher latitudes at 1 TeV than at 10 GeV. For reference, in Fig. 19 we show the individual HI and H<sub>2</sub> all-sky maps. In the case of bremsstrahlung, all structures are mostly determined by the distribution of H<sub>2</sub>, as this contributes the highest density in the Galactic plane, where CR  $e^\pm$  are densest. In contrast,  $\pi^0$ -decay emission exhibits structures from both H<sub>2</sub> and HI, where the high-latitude emission clearly follows the distribution of HI gas.

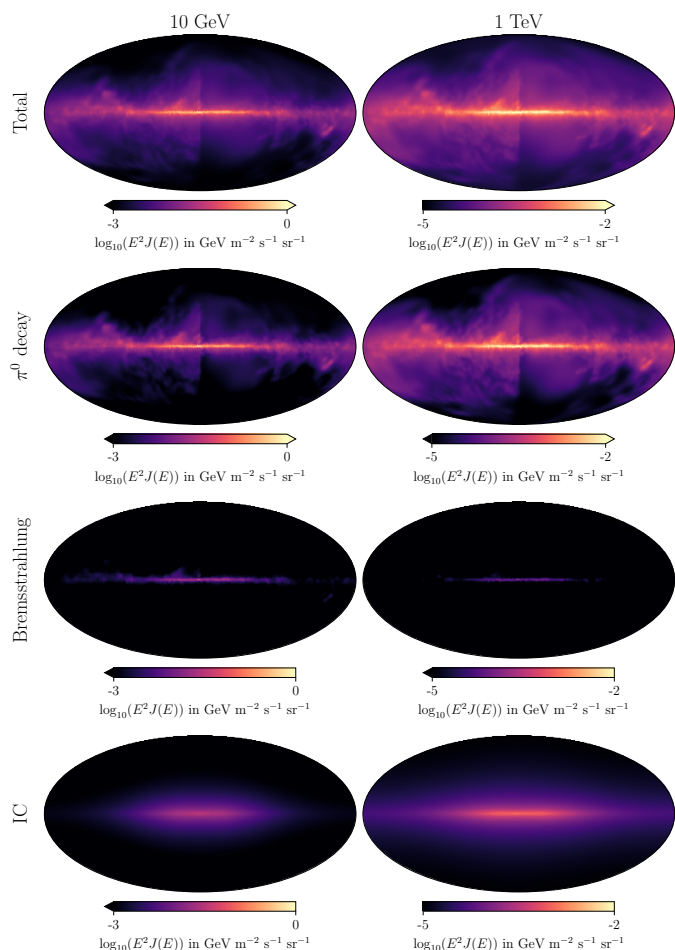


**Fig. 18.** All sky  $\gamma$ -ray emission for 3D model at 10 GeV (left) and 1 TeV (right). From top to bottom: Total,  $\pi^0$ -decay, bremsstrahlung, IC emission. Maps are shown for 10 GeV (left) and 1 TeV (right) energies.

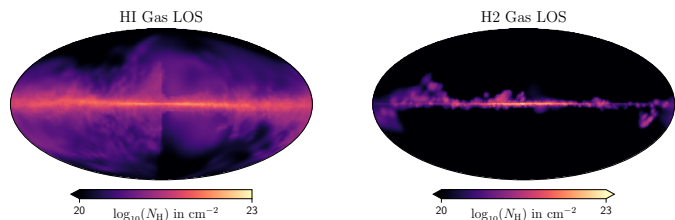


**Fig. 19.** All sky map for the individual HI (left) and  $H_2$  (right) gas reconstructions from the BEG03 model.

As the original gas reconstructions are defined on a Cartesian grid, the LOS projection is affected by the different angular resolution between nearby and distant gas structures. This effect is most obvious at high longitudes, where structures on the LOS projections are blurred out. At small longitudes the discrepancies between nearby and distant structures are less blurred. However, this also highlights prominent reconstructions artifacts such as the sharp jump seen at the GC.

In Fig. 20 we show  $\gamma$ -ray spectra from different locations in the sky. We particularly choose some star-forming regions and giant molecular clouds, alongside a high latitude under-dense region. Here, the locations in the sky where the total  $\gamma$  emission is highest are again proportional to the gas density, due to the dominance of  $\pi^0$ -decay emission. We see that the uncertainties become negligible, as they are defined for each voxel in the

3D gas distribution and have little effect after integrating along the LOS. Furthermore, we find that the spectral slope of the  $\gamma$ -ray spectra from dense regions like Aquila, the Cepheus Flare and the under-dense region at  $(l, b) = (300^\circ, 30^\circ)$  varies slightly, due to the contribution of IC emission. We see this in detail in Fig. 21 where we show the individual  $\gamma$ -ray emission channels along the LOS from the GC, Vela and the under-dense region at  $(l, b) = (300^\circ, 30^\circ)$ . Like for the specific emissivities, at the under-dense region, the spectral slope of IC emission varies with energy and IC emission itself is comparable to  $\pi^0$ -decay emission, though remaining always subdominant. We see that despite the local boost of bremsstrahlung emission at the GC, the integrated contribution from this direction does not dominate over IC emission.

#### 4. Summary and conclusions

We studied the impact of new 3D reconstructions of Galactic HI and  $H_2$  on our understanding of the CR transport and  $\gamma$ -ray emission. For this, we prepared a 2D and a 3D model, where the 2D model corresponds to an azimuthally-averaged version of the new gas maps interpolated to the simulation grid used, while the 3D model directly interpolates the new gas maps onto the simulation grid. Then, we solved the CR transport equation using PICARD for isotopes up to silicon. Finally, we used the corresponding transport results for the computation of Galactic diffuse  $\gamma$ -ray emission. For our simulations, we used 20 possible realizations of the new gas reconstruction to determine the impact of the uncertainties of the gas distribution at all stages of the simulations.

For CR transport, we found that, to account for a 3D structured gas distribution when fitting to B/C ratio data, the diffusion coefficient  $D_{xx}$  and Alfvén velocity  $v_a$  needed to be decreased in comparison to the 2D model, effectively reducing the diffusive strength. Furthermore, the rigidity dependence of the diffusion coefficient needed to be adjusted.

Next, we investigated the gas-induced structures in the distribution of different CR species, namely Boron, Carbon, protons and electrons. We observed that structures are gas-density, energy and CR-species dependent, where the different fragmentation and energy loss processes in the ISM lead to different imprints of gas in both primary and secondary species. We found a clear anti-correlation between gas density and CR fluxes for primaries at energies where diffusion does not dominate. In contrast, for secondaries there is a direct correlation between gas density and CR fluxes at all energies. This can clearly be seen by the energy-dependent Pearson correlation coefficient between protons/electrons and gas. We found that the uncertainties propagated from the uncertainties of the published gas distributions were negligible for the final CR distributions.

When comparing results of the axisymmetric model with the 3D model, we found a higher flux of primaries at low energies correlated to a smaller flux of secondaries at higher energies in the 3D model with respect to the 2D model. All of these effects were higher at the GC, where we noted that spectral differences come as a consequence of the distribution of gas structures, as local average gas densities remain equal.

Finally, we studied  $\gamma$ -ray emission produced from the simulated CR species both locally in the Galactic plane via the LOS integrals. In the Galactic plane, we observed a direct correlation between the total  $\gamma$ -ray emission and dense gas regions. We saw a high sensitivity to gas fluctuations arising in the 3D specific emissivity maps of  $\pi^0$ -decay and bremsstrahlung emission, as well as in the total emission. In locations of high gas

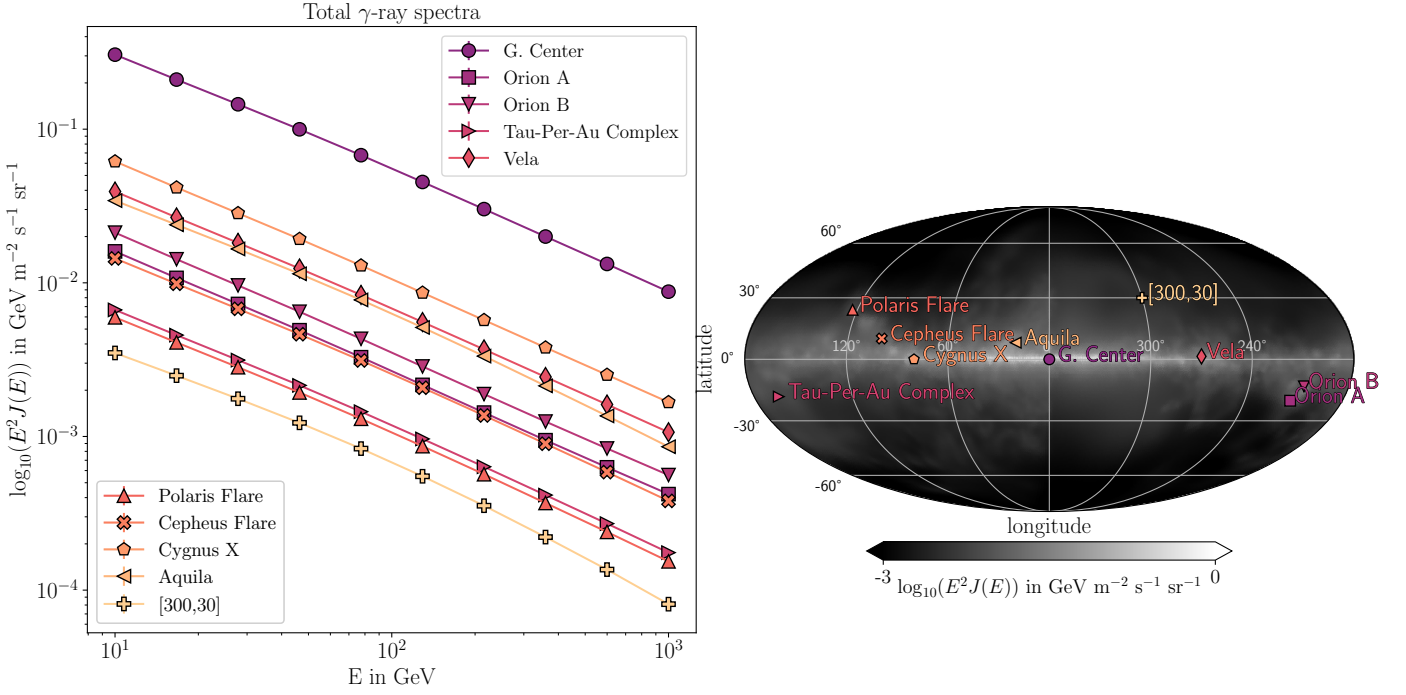


**Fig. 20.** *Left:* Total  $\gamma$ -ray spectra emitted from specific regions in the sky. *Right:* All-sky map for total  $\gamma$ -ray emission with the locations of the relevant regions highlighted.

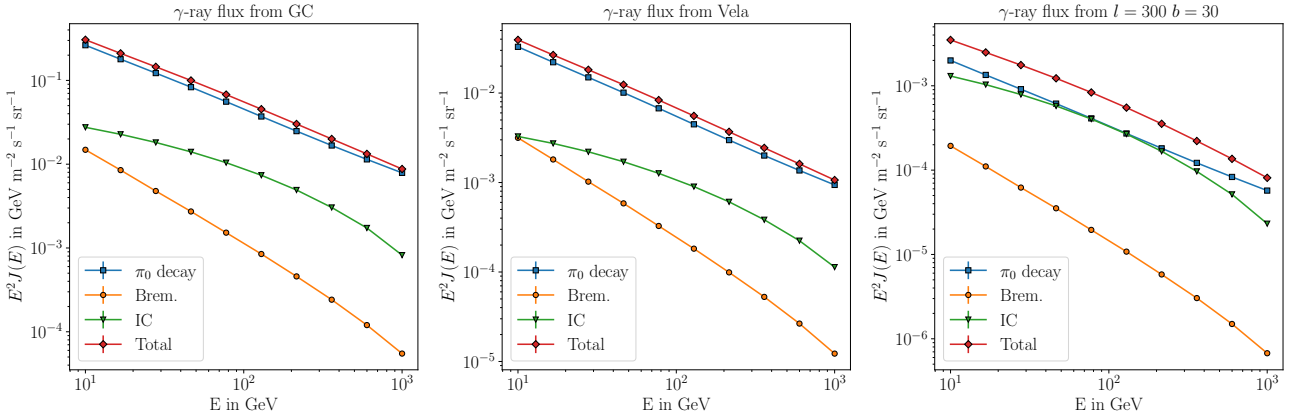


**Fig. 21.** Total and individual  $\gamma$ -ray spectra channels observed from Earth (left) Vela (middle) and at  $(l, b) = (300^\circ, 30^\circ)$ . Spectra follow by averaging the contribution within a disk of radius  $1^\circ$  around the relevant location.

density, the  $\pi^0$ -decay channel always remained dominant, with bremsstrahlung emission being boosted and dominating over IC emission in such regions, like the GC. In low gas-density regions, IC became dominant, conditional to a locally high ISRF. From the LOS-integrated emission, the structure of the total emission is fully determined by the gas maps. For the individual emission channels, gas structures on IC are smoothed out.

Due to the multiple effects through which ISM gas influences the distribution of CRs and  $\gamma$ -ray emission, as well as the influence of the gas structures themselves in diffusive transport, we strongly endorse the usage of 3D structured gas maps in 3D CR transport simulations.

*Acknowledgements.* Data used in this study was extracted with the help of the CRDB cosmic-ray database (Maurin et al. 2014, 2020, 2023). All figures in this publication have been created using *matplotlib* (Hunter 2007), where the *healpy* and *HEALPix* package were additionally used for some. Part of this work was supported by the German *Deutsche Forschungsgemeinschaft, DFG* project number 495252601. This research was funded in part, by the Austrian

Science Fund (FWF) [I 5925-N]. Gordian Edenhofer acknowledges that support for this work was provided by the German Academic Scholarship Foundation in the form of a PhD scholarship ("Promotionsstipendium der Studienstiftung des Deutschen Volkes"). Philipp Frank acknowledges funding through the German Federal Ministry of Education and Research for the project ErUM-IFT: Informationsfeldtheorie für Experimente an Großforschungsanlagen (Förderkennzeichen: 05D23EO1). Vo Hong Minh Phan acknowledges support from the Initiative Physique des Infinis (IPI), a research training program of the IDEX SUPER at Sorbonne Université.

## References

- Ackermann, M., Ajello, M., Atwood, W. B., et al. 2012, *ApJ*, 750, 3  
Adriani, O., Akaike, Y., Asano, K., et al. 2022, *Phys. Rev. Lett.*, 129, 251103  
Adriani, O., Barbarino, G. C., Bazilevskaia, G. A., et al. 2014, *ApJ*, 791, 93  
Aguilar, M., Ali Cavasonza, L., Alpat, B., et al. 2023, *Phys. Rev. Lett.*, 130, 211002  
Aguilar, M., Ali Cavasonza, L., Ambrosi, G., et al. 2018, *Phys. Rev. Lett.*, 120, 021101

- Arras, P., Baltac, M., Ensslin, T. A., et al. 2019, NIFTy5: Numerical Information Field Theory v5
- Beck, R. 2015, *A&A Rev.*, 24, 4
- Blasi, P. 2013, *A&A Rev.*, 21, 70
- Cerri, S. S., Gaggero, D., Vittino, A., Evoli, C., & Grasso, D. 2017, *J. Cosmology Astropart. Phys.*, 2017, 019
- Dampe Collaboration. 2022, *Science Bulletin*, 67, 2162
- DAMPE Collaboration. 2022, *Science Bulletin*, 67, 2162
- Edenhofer, G., Frank, P., Roth, J., et al. 2024, Re-Envisioning Numerical Information Field Theory (NIFTy.re): A Library for Gaussian Processes and Variational Inference
- Enßlin, T. A., Frommert, M., & Kitaura, F. S. 2009, *Phys. Rev. D*, 80, 105005
- Enßlin, T. A. 2019, *Annalen der Physik*, 531, 1800127
- Evoli, C., Amato, E., Blasi, P., & Aloisio, R. 2021, *Phys. Rev. D*, 104, 123029
- Evoli, C., Blasi, P., Amato, E., & Aloisio, R. 2020, *Phys. Rev. Lett.*, 125, 051101
- Evoli, C., Blasi, P., Morlino, G., & Aloisio, R. 2018, *Phys. Rev. Lett.*, 121, 021102
- Evoli, C., Gaggero, D., Vittino, A., et al. 2017, *Journal of Cosmology and Astroparticle Physics*, 2017, 015
- Evoli, C., Morlino, G., Blasi, P., & Aloisio, R. 2020, *Phys. Rev. D*, 101, 023013
- Farcy, M., Rosdahl, J., Dubois, Y., Blaizot, J., & Martin-Alvarez, S. 2022, *MNRAS*, 513, 5000
- Gabici, S. 2022, *A&A Rev.*, 30, 4
- Gabici, S., Evoli, C., Gaggero, D., et al. 2019, *International Journal of Modern Physics D*, 28, 1930022
- Génolini, Y., Serpico, P. D., Boudaud, M., et al. 2017, *Phys. Rev. Lett.*, 119, 241101
- Ghelfi, A., Maurin, D., Cheminet, A., et al. 2017, *Advances in Space Research*, 60, 833
- Giacinti, G. & Semikoz, D. 2023, arXiv e-prints, arXiv:2305.10251
- Girichidis, P., Pfrommer, C., Pakmor, R., & Springel, V. 2022, *MNRAS*, 510, 3917
- Grenier, I. A., Black, J. H., & Strong, A. W. 2015, *ARA&A*, 53, 199
- Haverkorn, M., Boulanger, F., Enßlin, T., et al. 2019, *Galaxies*, 7, 17
- Heinbach, U. & Simon, M. 1995, *ApJ*, 441, 209
- Hunter, J. D. 2007, *Computing in Science & Engineering*, 9, 90
- Jacobs, H., Mertsch, P., & Phan, V. H. M. 2022, *J. Cosmology Astropart. Phys.*, 2022, 024
- Jacobs, H., Mertsch, P., & Phan, V. H. M. 2023, *MNRAS*, 526, 160
- Jansson, R. & Farrar, G. R. 2012a, *ApJ*, 757, 14
- Jansson, R. & Farrar, G. R. 2012b, *ApJ*, 761, L11
- Jóhannesson, G., Porter, T. A., & Moskalenko, I. V. 2018, *ApJ*, 856, 45
- Kissmann, R. 2014, *Astroparticle Physics*, 55, 37
- Kissmann, R., Werner, M., Reimer, O., & Strong, A. 2015, *Astroparticle Physics*, 70, 39
- Maurin, D. 2020, *Computer Physics Communications*, 247, 106942
- Maurin, D., Ahlers, M., Dembinski, H., et al. 2023, *European Physical Journal C*, 83, 971
- Maurin, D., Dembinski, H. P., Gonzalez, J., Mariş, I. C., & Melot, F. 2020, *Universe*, 6, 102
- Maurin, D., Ferronato Bueno, E., & Derome, L. 2022, *A&A*, 667, A25
- Maurin, D., Melot, F., & Taillet, R. 2014, *A&A*, 569, A32
- Mertsch, P. 2020, *Ap&SS*, 365, 135
- Mertsch, P. & Phan, V. H. M. 2023, *A&A*, 671, A54
- Mertsch, P. & Vittino, A. 2021, *A&A*, 655, A64
- Moskalenko, I. V. & Strong, A. W. 1998, *ApJ*, 493, 694
- Moskalenko, I. V., Strong, A. W., Ormes, J. F., & Potgieter, M. S. 2002, *ApJ*, 565, 280
- Nakanishi, H. & Sofue, Y. 2003, *PASJ*, 55, 191
- Nakanishi, H. & Sofue, Y. 2006, *PASJ*, 58, 847
- Nava, L., Gabici, S., Marcowith, A., Morlino, G., & Ptuskin, V. S. 2016, *MNRAS*, 461, 3552
- Padovani, M., Ivlev, A. V., Galli, D., et al. 2020, *Space Sci. Rev.*, 216, 29
- Phan, V. H. M., Recchia, S., Mertsch, P., & Gabici, S. 2023, *Phys. Rev. D*, 107, 123006
- Pohl, M., Englmaier, P., & Bissantz, N. 2008, *ApJ*, 677, 283
- Porter, T. A., Jóhannesson, G., & Moskalenko, I. V. 2022, *The Astrophysical Journal Supplement Series*, 262, 30
- Schlickeiser, R. 2002, *Cosmic Ray Astrophysics*
- Selig, M., Bell, M. R., Junklewitz, H., et al. 2013, *A&A*, 554, A26
- Simpson, C. M., Pakmor, R., Pfrommer, C., Glover, S. C. O., & Smith, R. 2023, *MNRAS*, 520, 4621
- Skilling, J. 1975, *MNRAS*, 173, 255
- Steininger, T., Dixit, J., Frank, P., et al. 2019, *Annalen der Physik*, 531, 1800290
- Strong, A. W. & Moskalenko, I. V. 1998, *ApJ*, 509, 212
- Strong, A. W., Moskalenko, I. V., & Ptuskin, V. S. 2007a, *Annual Review of Nuclear and Particle Science*, 57, 285
- Strong, A. W., Moskalenko, I. V., & Ptuskin, V. S. 2007b, *Annual Review of Nuclear and Particle Science*, 57, 285
- Strong, A. W., Moskalenko, I. V., & Reimer, O. 2000, *ApJ*, 537, 763
- Tan, L. C. & Ng, L. K. 1983, *Journal of Physics G: Nuclear Physics*, 9, 227
- Thaler, J., Kissmann, R., & Reimer, O. 2023, *Astroparticle Physics*, 144, 102776
- Thomas, T. & Pfrommer, C. 2019, *MNRAS*, 485, 2977
- Thomas, T., Pfrommer, C., & Enßlin, T. 2020, *ApJ*, 890, L18
- Tibaldo, L., Gaggero, D., & Martin, P. 2021, *Universe*, 7, 141
- Yusifov, I. & Küçük, I. 2004, *A&A*, 422, 545